



SCUOLA INTERNAZIONALE SUPERIORE DI STUDI AVANZATI

SISSA Digital Library

Elastic Plateau-Rayleigh instability in soft cylinders: Surface elasticity and periodic beading

Original

Elastic Plateau-Rayleigh instability in soft cylinders: Surface elasticity and periodic beading / Magni, F., Riccobelli, D.. - In: JOURNAL OF THE MECHANICS AND PHYSICS OF SOLIDS. - ISSN 0022-5096. - 203:(2025). [10.1016/j.jmps.2025.106258]

Availability:

This version is available at: 20.500.11767/146850 since: 2025-07-09T05:24:30Z

Publisher:

Published

DOI:10.1016/j.jmps.2025.106258

Terms of use:

Testo definito dall'ateneo relativo alle clausole di concessione d'uso

Publisher copyright

note finali coverpage

(Article begins on next page)

ELASTIC PLATEAU–RAYLEIGH INSTABILITY IN SOFT CYLINDERS: SURFACE ELASTICITY AND PERIODIC BEADING

F. MAGNI* · D. RICCOBELLI†

Mathematics Area, mathLab, SISSA – International School for Advanced Studies

June 30, 2025

Abstract

The Plateau–Rayleigh instability shows that a cylindrical fluid flow can be destabilized by surface tension. Similarly, capillary forces can make an elastic cylinder unstable when the elastocapillary length is comparable to the cylinder’s radius. While existing models predict a single isolated bulge as the result of an instability, experiments reveal a periodic sequence of bulges spaced out by thinned regions, a phenomenon known as beading instability. Most models assume that surface tension is independent of the deformation of the solid, neglecting variations due to surface stretch.

In this work, we assume that surface tension arises from the deformation of material particles near the free surface, treating it as a pre-stretched elastic surface surrounding the body. Using the theoretical framework proposed by Gurtin and Murdoch, we show that a cylindrical solid can undergo a mechanical instability with a finite critical wavelength if the body is sufficiently soft or axially stretched. Post-buckling numerical simulations reveal a morphology in qualitative agreement with experimental observations. Period-halving secondary bifurcations are also observed. The results of this research have broad implications for soft materials, biomechanics, and microfabrication applications where surface tension plays a crucial role.

1 Introduction

A common observation, such as when tap water is gently opened, is that a thin, cylindrical stream of fluid can undergo a hydrodynamic instability. This instability causes the formation of sinusoidal bulges along the stream, which eventually break apart into droplets. This phenomenon is known as *Plateau–Rayleigh* instability: fluid-air surface tension tends to minimize the surface area, which leads to the formation of droplets (Plateau, 1873; Rayleigh, 1892).

Similarly to fluids, solids also possess a surface tension at the interface with other materials. While, for most solids, surface energy is negligible compared to the elastic energy of the object, when the material is very soft or small, capillarity becomes significant and can deform elastic solid bodies (Style et al., 2017; Bico et al., 2018). In particular, surface tension can induce large elastic deformations in soft solids, such as hydrogels filaments (Mora et al., 2013; Ang et al., 2020), rubber-like materials (Py et al., 2007; Elettro et al., 2016), and even biological matter (Riccobelli and Bevilacqua, 2020; Yadav et al., 2022; Ang et al., 2024; Riccobelli, 2025).

In recent years, several studies have investigated the classical counterparts of fluid-dynamical instabilities in solids, like the elastic Rayleigh–Taylor (Robinson and Swegle, 1989; Plohr and Sharp, 1998; Piriz et al., 2009; Mora et al., 2014; Riccobelli and Ciarletta, 2017) and Faraday (Shao et al., 2018; Bevilacqua et al., 2020; Shao et al., 2020).

Similarly, experiments show that elastic filaments can undergo a surface-tension-driven instability, resulting in a periodic sequence of bulges along the elastic body (Matsuo and Tanaka, 1992; Zuo et al., 2005; Naraghi et al., 2007; Mora et al., 2010), a phenomenon known as *beading*. This elastic analogue of the Plateau–Rayleigh instability has been investigated in recent years, see, for instance, Mora et al.

*fmagni@sissa.it

†davide.riccobelli@sissa.it

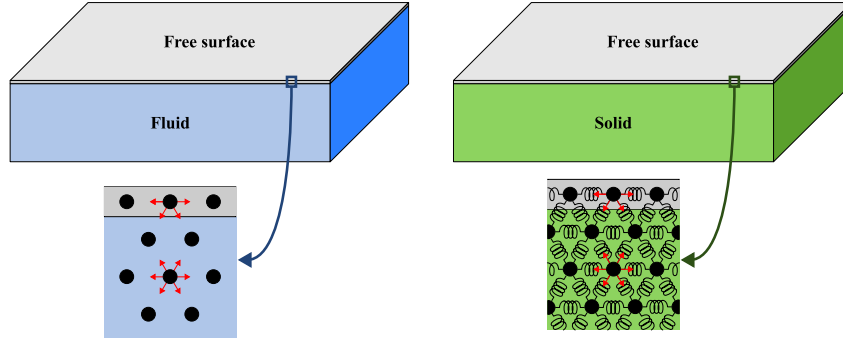


Figure 1: Surface tension in solids and fluids exhibits different constitutive responses. In fluids, it remains constant due to intermolecular forces, whereas in solids, deformation alters surface stress due to the elastic nature of intermolecular interactions.

(2010); Ciarletta and Ben Amar (2012); Taffetani and Ciarletta (2015b); Xuan and Biggins (2016), but existing theoretical models predict only the formation of an isolated bulge (Lestringant and Audoly, 2020; Fu et al., 2021).

Several studies have suggested that the experimentally observed finite wavelength may result from the sensitivity of the system to imperfections; see, for example, Taffetani and Ciarletta (2015a); Giudici and Biggins (2020). However, the experiments by Matsuo and Tanaka (Matsuo and Tanaka, 1992) demonstrate that the wavelength consistently scales with the radius of the cylinder. This scaling behavior indicates that wavelength selection is a robust and intrinsic feature of the instability, rather than a consequence of random surface imperfections. The occurrence of finite wavelength selection appears to be a common feature across several experiments, as reviewed in the introduction of Fu et al. (2021).

In most of the previously cited papers, surface tension in solids is treated as a constant quantity, similarly to fluids (Mora et al., 2010). Although this might be an acceptable approximation in many cases, studies have shown that surface tension in solids has an elastic nature, i.e. its value depends on the deformation of the surface, see fig. 1. The pioneering idea behind this phenomenon is due to Shuttleworth (1950), who postulated a linear dependence of the surface stress with respect to the surface deformation.

The inclusion of nonlinear elasticity effect in surface stress has been recently investigated in the context of the Plateau–Rayleigh instability by Bakiler et al. (2023) and Yu and Fu (2025), who proposed an additive decomposition of the surface stress into a constant term, equal to the classical surface tension in a fluid, and an elastic contribution. However, the resulting critical buckling mode still corresponds to an isolated bulge (Yu and Fu, 2025).

In this work, we present a different approach, modelling surface tension in solids as a pre-stretched elastic surface. Indeed, the rheology of fluids and solids is drastically different: particles close to the free surface are stretched by intermolecular cohesion forces, similarly to what happens in fluids, but this causes an elastic distortion of the material. Given the elastic nature of the body, this phenomenon is equivalent to imposing a pre-stretch on this thin layer of particles close to the surface. In the following, we explore how this different approach applies to the stability of cylindrical soft solids. Specifically, in Section 2 we propose a theoretical framework for pre-stretched elastic surfaces, building upon the work of Gurtin and Murdoch (1975). The proposed framework is specialized for a cylindrical geometry in Section 3. The linear stability of the system is analysed in Section 4 and a numerical post-buckling analysis is performed in Section 5.

2 Pre-stretched elastic surface surrounding an elastic solid

In this section, we present a mathematical theory of a three-dimensional elastic solid surrounded by an elastic surface subject to pre-stretch. The model is derived from the theoretical framework proposed by Gurtin and Murdoch (1975) and later extended by Holland et al. (2013) to account for morphoelastic phenomena.

2.1 Notation and basic kinematics

We consider a body with reference configuration \mathcal{B}_0 surrounded by a material surface $\mathcal{S}_0 = \partial\mathcal{B}_0$. Let χ be the deformation field mapping \mathcal{B}_0 to the current configuration \mathcal{B} . Similarly, the material reference surface \mathcal{S}_0 is mapped to its deformed counterpart \mathcal{S} via the surface deformation map χ_s , which represents the restriction of χ to the surface. We denote by $\mathcal{T}_{\mathbf{X}}$ and $\mathcal{T}_{\mathbf{x}}$ the tangent spaces to \mathcal{S}_0 in \mathbf{X} and to \mathcal{S} in \mathbf{x} respectively. Let $\mathbf{N}(\mathbf{X})$ and $\mathbf{n}(\mathbf{x})$ denote the outward normal of \mathcal{S}_0 in \mathbf{X} and of \mathcal{S} in \mathbf{x} , respectively. We introduce the surface identity tensors

$$\mathbf{l}_s(\mathbf{X}) = \mathbf{l}(\mathbf{X}) - \mathbf{N}(\mathbf{X}) \otimes \mathbf{N}(\mathbf{X}), \quad (1)$$

$$\mathbf{H}_s(\mathbf{x}) = \mathbf{l}(\mathbf{x}) - \mathbf{n}(\mathbf{x}) \otimes \mathbf{n}(\mathbf{x}), \quad (2)$$

where \mathbf{l} is the identity tensor. We can now define the bulk and the surface deformation gradient as

$$\mathbf{F} = \nabla\chi, \quad \mathbf{F}_s = \mathbf{F}\mathbf{l}_s, \quad (3)$$

where ∇ denotes the gradient operator using referential coordinates. Similarly, we introduce a surface determinant operator, indicated with \det_s , that accounts for the local area change induced by \mathbf{F}_s , see appendix A. In this respect, we set

$$J_s := \det_s \mathbf{F}_s; \quad (4)$$

see Appendix A for a definition of the surface determinant and some recalls on differential calculus on material surfaces.

Since \mathbf{l}_s is a rank-deficient tensor, the surface deformation gradient \mathbf{F}_s is non-invertible. To overcome this issue, we introduce a generalized inverse for a general rank-deficient tensor \mathbf{A} following Holland et al. (2013). To this end, we exploit the singular value decomposition

$$\mathbf{A} = \mathbf{V}\Sigma\mathbf{W}^T, \quad (5)$$

where Σ is a diagonal tensor whose diagonal components correspond to the singular values of \mathbf{A} , while \mathbf{V} and \mathbf{W} represent the tensors whose columns are the left- and right-singular vectors, respectively. The generalized inverse can be defined as

$$\mathbf{A}^{-1} = \mathbf{W}[\Sigma^+]^{-1}\mathbf{V}^T, \quad (6)$$

where $[\Sigma^+]^{-1}$ is the pseudoinverse of Σ obtained by substituting each non-zero entry on the diagonal of Σ with its reciprocal value. By construction, we observe that (Yu and Fu, 2025; Javili et al., 2014)

$$\mathbf{F}_s^{-1}\mathbf{F}_s = \mathbf{l}_s, \quad \mathbf{F}_s\mathbf{F}_s^{-1} = \mathbf{H}_s.$$

We are now ready to describe the mechanics of elastic surfaces.

2.2 Pre-stretched elastic surfaces: balance equations

In what follows, we present a model of pre-stretched elastic surfaces surrounding a three-dimensional continuum. To this end, inspired by the work of Holland et al. (2013), we can perform a multiplicative decomposition of the surface deformation gradient in a similar fashion as is done in bulk elasticity

$$\mathbf{F}_s = \mathbf{F}_s^e \mathbf{F}_s^p, \quad (7)$$

where \mathbf{F}_s^p accounts for the elastic pre-stretch, while \mathbf{F}_s^e is the elastic distortion from the relaxed state to the current configuration. Specifically, \mathbf{F}_s^p describes the local distortion of each point on the referential surface to its relaxed state, see fig. 2.

We assume quasistatic deformations, so that inertia terms can be neglected. Let \mathbf{P}_s be the first surface Piola-Kirchhoff stress tensor and \mathbf{b}_0 the density of body force per unit referential area. From the balance of forces we obtain (Gurtin and Murdoch, 1975)

$$\nabla_s \cdot \mathbf{P}_s + \mathbf{b}_s = \mathbf{P}\mathbf{N} \quad \text{on } \mathcal{S}_0, \quad (8)$$

where \mathbf{P} is the (bulk) Piola-Kirchhoff stress tensor, while $\nabla_s \cdot$ denotes the surface divergence operator (see Appendix A for a definition). We remark that eq. (8) provides the boundary condition for the classical balance equation of linear momentum of a three dimensional body

$$\nabla \cdot \mathbf{P} + \mathbf{b} = \mathbf{0}. \quad (9)$$

In isothermal conditions, if we assume the existence of a surface strain energy density per unit reference area $\psi_s = \psi_s(\mathbf{F}_s)$, standard thermodynamic considerations allow us to write (Deghghany et al., 2020)

$$\mathbf{P}_s = \frac{\partial \psi_s}{\partial \mathbf{F}_s}. \quad (10)$$

This equation characterizes hyperelastic material surfaces, similarly to classical hyperelastic materials. In order to construct the strain energy density of the material in the presence of a pre-stretch, a careful treatment is required.

The boundary layer generated by capillary forces is very small, so we are allowed to consider only stretching effects and neglect bending energy, as in the theoretical framework of Gurtin and Murdoch (1975). It is important to track the variations of the thickness of the material surface in the process. We assume that the material surface represents the limit of a thin layer of a three-dimensional incompressible material. Let H and H_r be the (infinitesimal) thicknesses of the material surface in the reference and in the relaxed state, respectively. We recall that $\det_s \mathbf{F}_s^p$ describes the change in surface area from the reference to the relaxed state, so that

$$dS_r = \det_s \mathbf{F}_s^p dS, \quad (11)$$

where dS_r and dS are the infinitesimal area element in the relaxed and reference state, respectively. Thus, from the incompressibility of the material we have

$$H = H_r \det_s \mathbf{F}_s^p.$$

We consider the strain energy density ψ_s^r per unit surface area in the relaxed state. We introduce W_s^r , defined as

$$W_s^r(\mathbf{F}_s^e) := \frac{\psi_s^r(\mathbf{F}_s^e)}{H_r}.$$

Here, W_s^r can be regarded as strain energy density per unit volume averaged across the material surface thickness. By eq. (11), introducing $\psi_{s0}(\mathbf{F}_s^e) = W_s^r(\mathbf{F}_s^e) H$, we get

$$\psi_s^r(\mathbf{F}_s(\mathbf{F}_s^p)^{-1}) dS_r = \psi_{s0}(\mathbf{F}_s(\mathbf{F}_s^p)^{-1}) dS = \psi_s(\mathbf{F}_s) dS.$$

Therefore, a direct computation shows that

$$\mathbf{P}_s = \frac{\partial \psi_{s0}}{\partial \mathbf{F}_s^e} (\mathbf{F}_s^e)^{-T}. \quad (12)$$

We can now specialize this framework to a solid cylinder coated by a pre-stretched membrane.

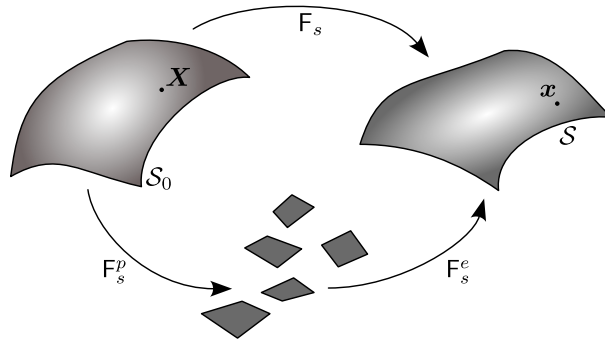


Figure 2: Representation of the multiplicative decomposition of the surface deformation gradient tensor $\mathbf{F}_s = \mathbf{F}_s^e \mathbf{F}_s^p$.

3 Solid elastic cylinder surrounded by a pre-tensioned elastic surface

Let $\mathcal{B}_0 \subset \mathbb{R}^3$ be the reference configuration representing the cylinder, with R_0 denoting its radius. We introduce the referential cylindrical coordinates (R, Θ, Z) and the corresponding vector basis $(\mathbf{E}_R, \mathbf{E}_\Theta, \mathbf{E}_Z)$. We assume that its axial length is much greater than the radius, so that we can assume \mathcal{B}_0 to be infinite in the direction \mathbf{E}_Z .

We introduce the current position $\mathbf{x} \in \mathcal{B} \subset \mathbb{R}^3$ of a point \mathbf{X} , where $\mathbf{x} = \chi(\mathbf{X})$ and $\mathcal{B} = \chi(\mathcal{B}_0)$ is the current configuration of the cylinder. Moreover, let (r, θ, z) be the cylindrical coordinate system in the current configuration. The corresponding orthonormal basis vectors is given by $(\mathbf{e}_r, \mathbf{e}_\theta, \mathbf{e}_z)$. We denote by $\mathbf{u} : \mathcal{B}_0 \rightarrow \mathbb{R}^3$ the displacement field, so that $\mathbf{x}(\mathbf{X}) = \chi(\mathbf{X}) = \mathbf{X} + \mathbf{u}(\mathbf{X})$. The cylinder is free of body forces, so that the balance equations (8) and (9) become

$$\nabla \cdot \mathbf{P} = \mathbf{0} \quad \text{in } \mathcal{B}_0, \quad (13a)$$

$$\nabla_s \cdot \mathbf{P}_s = \mathbf{P}N \quad \text{on } \mathcal{S}_0. \quad (13b)$$

Furthermore, we assume that the system is elongated by a mean stretch λ acting along the Z direction.

In order to proceed with our analysis we have to make some constitutive assumptions. The material composing the cylinder volume is assumed to be incompressible, implying

$$J := \det \mathbf{F} = 1. \quad (14)$$

We take a neo-Hookean volumetric strain energy density, so that

$$\psi = \frac{\mu}{2} (I_1 - 3), \quad (15)$$

where μ is the bulk shear modulus and $I_1 = \text{tr}(\mathbf{F}^T \mathbf{F})$.

We assume that the elastic surface is isotropically stretched with

$$\mathbf{F}_s^p = \lambda_p \mathbf{I}_s, \quad (16)$$

where λ_p is the stretch from the reference to the relaxed state of the body, see fig. 2. Here, we assume that $\lambda_p \in (0, 1]$ so that the elastic surface is under tension. The case $\lambda_p = 1$ corresponds to the absence of surface stress in the reference configuration.

As a surface strain energy density, we use

$$\psi_{s0}(\mathbf{F}_s^e) = \frac{\mu_s}{2} \left(I_s^e - 2 - 2 \ln J_e \right) + \frac{\Lambda_s}{2} \left(\frac{1}{2} (J_e^2 - 1) - \ln J_e \right), \quad (17)$$

where μ_s is the surface shear modulus and Λ_s modulates surface extensibility (the higher Λ_s , the more inextensible). The quantity I_s^e is defined as $I_s^e = \text{tr} \left((\mathbf{F}_s^e)^T \mathbf{F}_s^e \right)$, while $J_e = \det_s \mathbf{F}_s^e$ represents the elastic part of the surface Jacobian J_s .

Since we are dealing with hyperelastic materials, the bulk Piola-Kirchhoff stress tensor is given by

$$\mathbf{P} = \frac{\partial \psi}{\partial \mathbf{F}} - p \mathbf{F}^{-T} = \mu \mathbf{F} - p \mathbf{F}^{-T}, \quad (18)$$

where p , usually called pressure, is a Lagrange multiplier introduced to enforce the incompressibility constraint.

Assuming the multiplicative decomposition (5) for \mathbf{F}_s and using eq. (12), we obtain the following expression for the surface Piola-Kirchhoff stress tensor

$$\mathbf{P}_s = \mu_s \left(\mathbf{F}_s (\mathbf{F}_s^p)^{-1} (\mathbf{F}_s^p)^{-T} - \mathbf{F}_s^{-T} \right) + \frac{\Lambda_s}{2} \left(\frac{J_s}{J_s^p} - 1 \right) \mathbf{F}_s^{-T}. \quad (19)$$

Remark 1. *In the undeformed reference configuration, i.e. when $\mathbf{F} = \mathbf{I}$, the surface stress \mathbf{P}_s corresponds to an isotropic surface stress, as in fluids, so that*

$$\mathbf{P}_s = \gamma \mathbf{I}_s.$$

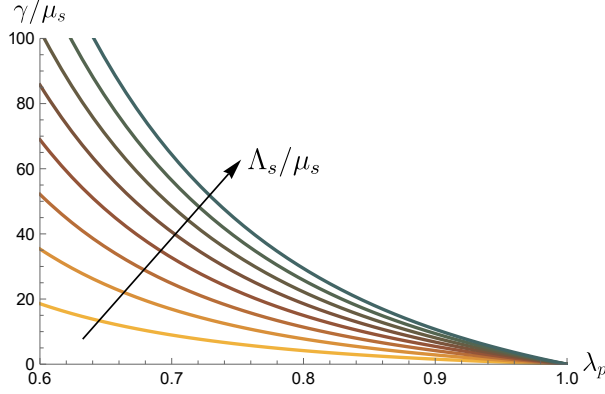


Figure 3: Plot of the surface tension γ in the reference configuration, nondimensionalized with respect to the surface shear modulus μ_s , as a function of the pre-stretch parameter λ_p for $\Lambda_s/\mu_s = 5, 10, \dots, 40$. The ratio Λ_s/μ_s represents the relative importance of surface extensibility with respect to shear stresses: the higher it is, the more under tension the surface is. The arrow denotes the direction in which Λ_s/μ_s grows.

We call γ initial surface tension. It is a function of λ_p and the material parameters μ_s and Λ_s , specifically

$$\gamma = \frac{1 - \lambda_p^4}{2\lambda_p^4} \Lambda_s + \frac{1 - \lambda_p^2}{\lambda_p^2} \mu_s. \quad (20)$$

In particular, the surface is under tension for $0 < \lambda_p < 1$, see fig. 3. For small deformations from the reference configuration, the stress \mathbf{P}_s obeys to the Shuttleworth equation, as discussed by Yu and Fu (2025), with the initial surface tension γ given by eq. (20).

In the next section, we show that the cylinder can undergo a beading instability when subjected to a homogeneous uniaxial stretch.

4 Stability analysis

In this section we conduct a linear stability analysis of the cylindrical configurations with respect to axisymmetric perturbations with a wavenumber k . In what follows, we show that the body always admits a cylindrical solution, and we perform a stability analysis. Readers mainly interested in results are suggested to go directly to section 4.4.

4.1 Cylindrical solution

Cylindrical solutions representing homogeneous uniaxial extensions are represented by the following class of deformations

$$r = \frac{R}{\sqrt{\lambda}}, \quad z = \lambda Z, \quad (21)$$

which satisfies the incompressibility constraint (14). Indeed, the deformation gradient associated to eq. (21) is given by

$$\mathbf{F} = \lambda^{-\frac{1}{2}} (\mathbf{e}_r \otimes \mathbf{E}_R + \mathbf{e}_\theta \otimes \mathbf{E}_\Theta) + \lambda \mathbf{e}_z \otimes \mathbf{E}_Z.$$

The corresponding surface deformation gradient can be obtained through eq. (3), so that

$$\mathbf{F}_s = \lambda^{-\frac{1}{2}} \mathbf{e}_\theta \otimes \mathbf{E}_\Theta + \lambda \mathbf{e}_z \otimes \mathbf{E}_Z.$$

From eq. (18), we compute the bulk Piola-Kirchhoff stress tensor

$$\mathbf{P} = \left(\frac{\mu}{\sqrt{\lambda}} - \sqrt{\lambda} p \right) (1 - \mathbf{e}_z \otimes \mathbf{E}_Z) + \left(\lambda \mu - \frac{p}{\lambda} \right) \mathbf{e}_z \otimes \mathbf{E}_Z \quad (22)$$

and its surface counterpart through eq. (19)

$$\mathbf{P}_s = \left(\frac{1}{2} \left(\frac{\lambda^{3/2}}{\lambda_p^4} - \sqrt{\lambda} \right) \Lambda_s + \left(\frac{1}{\sqrt{\lambda} \lambda_p^2} - \sqrt{\lambda} \right) \mu_s \right) \mathbf{e}_\theta \otimes \mathbf{E}_\Theta + \left(\frac{1}{2} \left(\frac{1}{\lambda_p^4} - \frac{1}{\lambda} \right) \Lambda_s + \left(\frac{\lambda}{\lambda_p^2} - \frac{1}{\lambda} \right) \mu_s \right) \mathbf{e}_z \otimes \mathbf{E}_Z. \quad (23)$$

Finally, we can find the expression of the pressure field p by enforcing the boundary condition eq. (13b). Using eqs. (22) and (23) we get

$$P_{RR} = -\frac{P_s \Theta \Theta}{R_0}.$$

By solving this equation with respect to p we obtain

$$p = \frac{2\lambda_p^2 (\mu R_0 \lambda_p^2 + \mu_s) - \lambda \lambda_p^4 (\Lambda_s + 2\mu_s) + \lambda^2 \Lambda_s}{2\lambda R_0 \lambda_p^4}. \quad (24)$$

We can now investigate possible bifurcations of the cylindrical configuration that can eventually lead to a beading instability.

4.2 Incremental relations

We make use of the theory of incremental deformations to analyse the linear stability of the cylindrical configuration (Ogden, 1997). We introduce the incremental displacement and pressure fields, denoted by $\delta \mathbf{u} : \mathcal{B} \rightarrow \mathbb{R}^3$ and $\delta p : \mathcal{B} \rightarrow \mathbb{R}$, respectively. We set $\Gamma := \text{grad } \delta \mathbf{u}$.

Similarly, let Γ_s be the surface gradient of the incremental displacement, so that $\Gamma_s = \Gamma \mathbf{H}_s$. The bulk and surface incremental Piola-Kirchhoff stress tensors are given by (Yu and Fu, 2025)

$$\begin{aligned} \delta \mathbf{P} &= \mathcal{A}_0 : \Gamma + p \Gamma^T - \delta p \mathbf{I}, & \text{so that} & & \delta P_{ij} &= \mathcal{A}_{0ijhk} \Gamma_{hk} + p \Gamma_{ji} - \delta p I_{ij}, \\ \delta \mathbf{P}_s &= \mathcal{C}_0 : \Gamma_s, & & & \delta P_{sij} &= \mathcal{C}_{0ijhk} \Gamma_{shk}. \end{aligned} \quad (25)$$

where \mathcal{A}_0 and \mathcal{C}_0 are the fourth-order tensors of the bulk and surface instantaneous elastic moduli, respectively. Their components are given by

$$\mathcal{A}_{0ijhk} = F_{jm} F_{kn} \frac{\partial^2 \psi}{\partial F_{im} \partial F_{hn}}, \quad (26a)$$

$$\mathcal{C}_{0ijhk} = J_s^{-1} F_{jm}^s F_{kn}^s \frac{\partial^2 \psi_s}{\partial F_{im}^s \partial F_{hn}^s}, \quad (26b)$$

where we assume summation over repeated indices. The incremental counterpart of eqs. (13a) and (13b) and eq. (14) are given by

$$\text{div } \delta \mathbf{P} = \mathbf{0} \quad \text{in } \mathcal{B}, \quad (27a)$$

$$\text{tr } \Gamma = 0 \quad \text{in } \mathcal{B}, \quad (27b)$$

$$\text{div}_s \delta \mathbf{P}_s = \delta \mathbf{P} \mathbf{n} \quad \text{on } \mathcal{S}. \quad (27c)$$

If the material is isotropic, a convenient way of computing the components of the tensors \mathcal{A}_0 and \mathcal{C}_0 is to rely on the principal stretches, indicated in this case by $\lambda_r = \lambda_\theta = \lambda^{-1/2}$ and $\lambda_z = \lambda$. Indeed, by using cylindrical coordinates with $i, j \in \{r, \theta, z\}$ and $\alpha, \beta \in \{\theta, z\}$ we get (Ogden, 1997)

$$\mathcal{A}_{0iijj} = \lambda_i \lambda_j \psi_{,ij}, \quad (28a)$$

$$\mathcal{A}_{0jiji} = \frac{\lambda_i^2}{\lambda_i^2 - \lambda_j^2} (\lambda_i \psi_{,i} - \lambda_j \psi_{,j}) \quad \text{if } i \neq j, \quad (28b)$$

$$\mathcal{A}_{0ijji} = \mathcal{A}_{0jiii} = \mathcal{A}_{0jiji} - \lambda_i \psi_{,i} \quad \text{if } i \neq j, \quad (28c)$$

while, for the surface elastic moduli we obtain (Yu and Fu, 2025; Chadwick and Ogden, 1971)

$$\begin{aligned}
J_s \mathcal{C}_{0\alpha\alpha\beta\beta} &= \lambda_\alpha \lambda_\beta \psi_{s,\alpha\beta}, \\
J_s \mathcal{C}_{0\beta\alpha\beta\alpha} &= \frac{\lambda_\alpha^2}{\lambda_\alpha^2 - \lambda_\beta^2} (\lambda_\alpha \psi_{s,\alpha} - \lambda_\beta \psi_{s,\beta}) \quad \text{if } \alpha \neq \beta, \\
J_s \mathcal{C}_{0\beta\alpha\alpha\beta} &= \frac{\lambda_\alpha \lambda_\beta}{\lambda_\alpha^2 - \lambda_\beta^2} (\lambda_\beta \psi_{s,\alpha} - \lambda_\alpha \psi_{s,\beta}) \quad \text{if } \alpha \neq \beta, \\
J_s \mathcal{C}_{0r\alpha r\alpha} &= \lambda_\alpha \psi_{s,\alpha}.
\end{aligned}$$

4.3 Axisymmetric solutions of the incremental problem and linear stability analysis

We can now proceed with the solution of the incremental problem (27) and the construction of a bifurcation criterion.

While an axially compressed cylinder can undergo a non-axisymmetric instability, similarly to the classical Euler buckling problem (Goriely et al., 2008), in the presence of surface tension and axial traction the buckling mode is axisymmetric (Mora et al., 2010; Fu et al., 2021). Therefore, in the following we focus on axisymmetric perturbations to the base solution, i.e. we assume that the incremental displacement $\delta \mathbf{u}$ and the incremental pressure δp have the following structure:

$$\delta \mathbf{u} = u(r, z) \mathbf{e}_r + w(r, z) \mathbf{e}_z, \quad \delta p = \delta p(r, z). \quad (29)$$

By exploiting a matrix representation of second order tensors through the cylindrical basis, we can write the gradient of the incremental displacement as

$$\Gamma = \text{grad } \delta \mathbf{u} = \begin{pmatrix} \frac{\partial u}{\partial r} & 0 & \frac{\partial u}{\partial z} \\ 0 & \frac{u}{R} & 0 \\ \frac{\partial w}{\partial r} & 0 & \frac{\partial w}{\partial z} \end{pmatrix}. \quad (30)$$

The surface counterpart of Γ can be obtained through eq. (2), so that

$$\Gamma_s = \Gamma \mathbf{H}_s = \begin{pmatrix} 0 & 0 & \frac{\partial u}{\partial Z} \\ 0 & \frac{u}{R} & 0 \\ 0 & 0 & \frac{\partial w}{\partial Z} \end{pmatrix}.$$

In order to proceed with the analysis, we assume the following separation of variables

$$u(r, z) = U(r) \sin(kz), \quad (31a)$$

$$w(r, z) = W(r) \cos(kz), \quad (31b)$$

$$\delta p(r, z) = Q(r) \sin(kz), \quad (31c)$$

where k is the wavenumber of the perturbation. Hence, we can obtain $W(r)$ and $Q(r)$ as a function of $U(r)$ and its derivatives from eq. (27b) and the expression of δP_{rr} in eq. (25), respectively, so that

$$\begin{aligned}
W(r) &= \frac{rU'(r) + U(r)}{kr}, \\
Q(r) &= \frac{\mu \left(r \left(r \left(rU^{(3)}(r) + 2U''(r) \right) - (k^2 \lambda^3 r^2 + 1) U'(r) \right) + U(r) (1 - k^2 \lambda^3 r^2) \right)}{k^2 \lambda r^3}.
\end{aligned}$$

From eq. (27a), we finally obtain a fourth order ordinary differential equation for $U(r)$:

$$\begin{aligned}
&\frac{r \left((k^2 (\lambda^3 + 1) r^2 - 3) U'(r) + r \left((k^2 (\lambda^3 + 1) r^2 + 3) U''(r) - r \left(rU^{(4)}(r) + 2U'''(r) \right) \right) \right)}{k^2 \lambda r^4} + \\
&\quad - \frac{U(r) \left(k^4 \lambda^3 r^4 + k^2 (\lambda^3 + 1) r^2 - 3 \right)}{k^2 \lambda r^4} = 0.
\end{aligned} \quad (32)$$

The general solution of eq. (32) for $U(r)$, ensuring the continuity of the body along the cylinder's axis, is given by a linear combination of two independent functions, $U_1(r)$ and $U_2(r)$ (Bigoni and Gei, 2001), i.e.

$$U(r) = c_1 U_1(r) + c_2 U_2(r), \quad (33)$$

where c_1 and c_2 are arbitrary constants. In particular, when $\lambda \neq 1$,

$$U_1(r) = J_1(kr q_1) \quad U_2(r) = J_1(kr q_2), \quad (34)$$

where J_m is the modified Bessel function of the first kind of order m , while q_1 and q_2 are two coefficients given by

$$q_{1,2}^2 = \frac{\lambda^3 + 1 \pm (\lambda^3 - 1)}{2}. \quad (35)$$

Instead, if $\lambda = 1$, we get (Bigoni and Gei, 2001)

$$U_1(r) = J_1(kr), \quad U_2(r) = r J_0(kr). \quad (36)$$

We are now left with the imposition of the boundary condition eq. (27c). Given the solution eq. (33), such a boundary condition reduces to a linear system whose unknowns are $(c_1, c_2) = \mathbf{c}$, i.e.

$$\mathbf{M}\mathbf{c} = \mathbf{0}.$$

Here, \mathbf{M} is a 2×2 matrix whose elements are reported in appendix B.

Non-trivial solutions of the incremental problem exist when the matrix \mathbf{M} is singular, that is

$$\varphi(k, \mu, \lambda, \mu_s, \Lambda_s, \lambda_p, R_0) := \det \mathbf{M} = 0. \quad (37)$$

Equation (37) is highly nonlinear and it is not possible to find analytic expressions for the roots. Thus, we rely on numerical computations to find its solutions, using a Newton algorithm implemented with the software `Mathematica 13.3` (Wolfram Research, Champaign, IL, USA).

In the following section we perform a non-dimensionalization of eq. (37) and present and discuss the results of the linear stability analysis.

4.4 Results of the linear stability analysis

First, we identify the non-dimensional quantities that govern the behaviour of the system. In particular, we choose R_0 and μ_s as characteristic length and stiffness of the system, respectively. This choice allows us to identify the following dimensionless quantities

$$\widehat{\mu} = \frac{\mu R_0}{\mu_s}, \quad \widehat{\Lambda}_s = \frac{\Lambda_s}{\mu_s}, \quad \widehat{k} = k R_0,$$

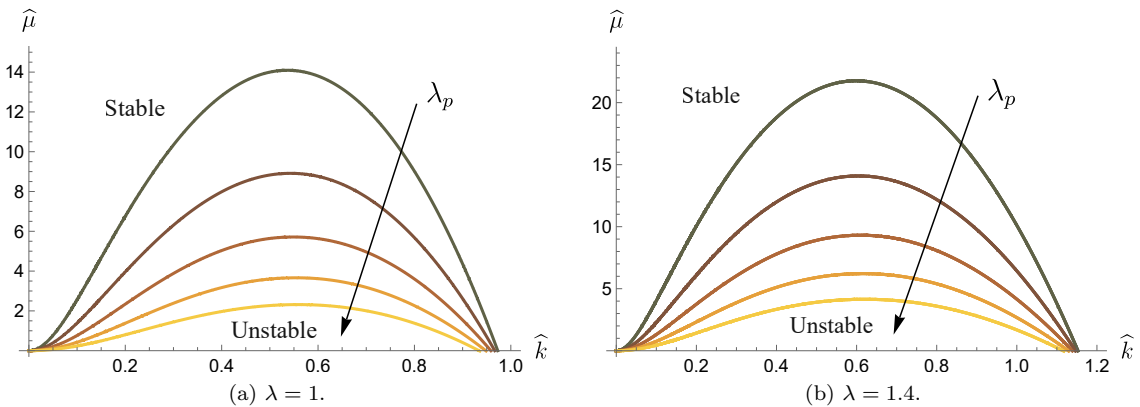


Figure 4: Plot of the dimensionless shear modulus $\widehat{\mu}$ versus the dimensionless wave number \widehat{k} for unitary (fig. 4a) and nonunitary (fig. 4b) axial strain, respectively. Here, the dimensionless surface extensibility $\widehat{\Lambda}_s$ is set to 40 and the pre-stretch parameter $\lambda_p = 0.4, 0.5, 0.6, 0.7, 0.8$. The arrow denotes the direction of growth of λ_p .

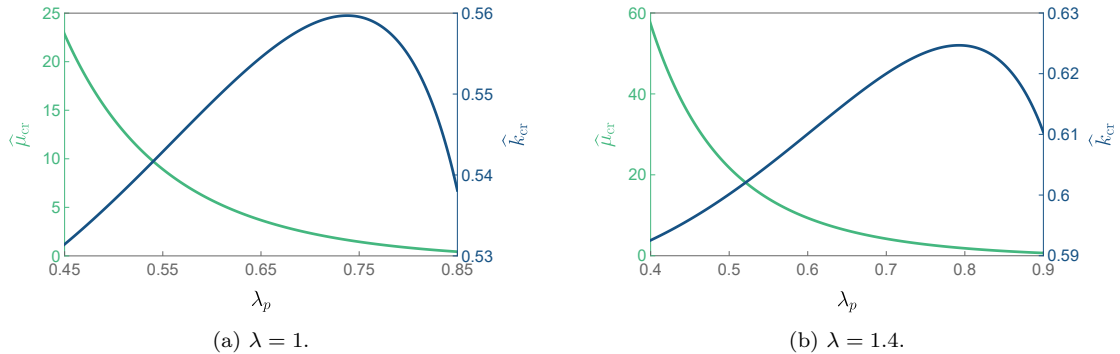


Figure 5: Plot of the critical bifurcation thresholds of the dimensionless shear modulus $\hat{\mu}_{\text{cr}}$ (turquoise) and of the dimensionless wavenumber \hat{k}_{cr} (blue) against the pre-stretch parameter λ_p for unitary (fig. 5a) and nonunitary (fig. 5b) axial strain, respectively. Here, the dimensionless surface extensibility $\hat{\Lambda}_s$ is set to 40.

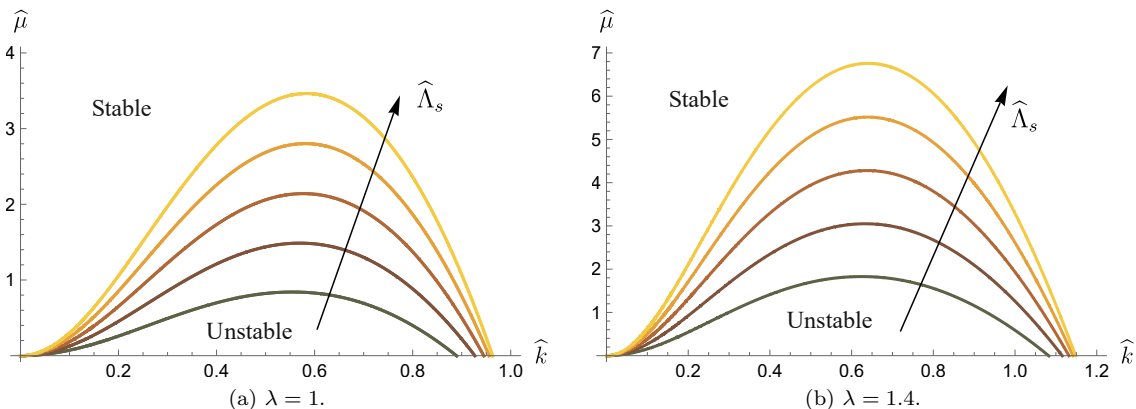


Figure 6: Plot of the dimensionless shear modulus $\hat{\mu}$ versus the dimensionless wave number \hat{k} for unitary (fig. 6a) and nonunitary (fig. 6b) axial strain, respectively. Here, the pre-stretch parameter λ_p is set to 0.8 and the dimensionless surface extensibility $\hat{\Lambda}_s = 40, 60, 80, 100, 120$. The arrow denotes the direction of growth of $\hat{\Lambda}_s$.

representing the dimensionless shear modulus, the dimensionless surface extensibility, and the dimensionless wavenumber, respectively. We observe that μ_s/μ can be interpreted as the counterpart of the classical elasto-capillary length of the system (Style et al., 2017), while $\hat{\Lambda}_s$ measures the extensibility of the free surface.

In the following, we refer to the first mode that becomes unstable as the critical buckling mode. The corresponding dimensionless critical wavenumber is denoted by \hat{k}_{cr} .

We first explore the stability of the cylindrical configuration with respect to control parameter $\hat{\mu}$, analysing the effect of surface pre-stretch. In all the studied cases, as we decrease $\hat{\mu}$, the critical mode has a non-zero wavenumber, see fig. 4. The marginal stability curves in fig. 4 show a similar trend as we change the parameters. Specifically, we observe a decrease in the critical thresholds for $\hat{\mu}$ as λ_p approaches 1. Moreover, axial stretching appears to stabilize the cylinder: a bifurcation occurs at larger values of $\hat{\mu}$ when $\lambda = 1.4$ with respect to the case with $\lambda = 1$, as shown in fig. 4. In fig. 5 we report the trend of the critical wavenumber and of the critical shear modulus. Our results show that $\hat{\mu}_{\text{cr}}$ monotonically decreases as λ_p increases.

We now analyse the effect of surface extensibility. The results are reported in fig. 6. As the surface becomes less extensible, i.e. as $\hat{\Lambda}_s$ grows, also $\hat{\mu}_{\text{cr}}$ monotonically grows. From fig. 7 we can notice that this trend is linear for both $\lambda = 1$ and $\lambda = 1.4$. In particular, the axial strain has a stabilizing effect

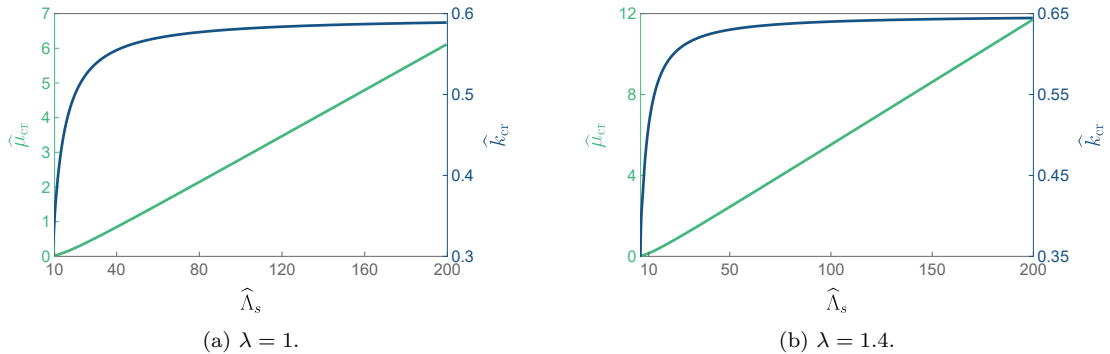


Figure 7: Plot of the critical bifurcation thresholds of the dimensionless shear modulus $\hat{\mu}_{\text{cr}}$ (turquoise) and of the dimensionless wavenumber \hat{k}_{cr} (blue) against the dimensionless surface extensibility $\hat{\Lambda}_s$ for unitary (fig. 7a) and nonunitary (fig. 7b) axial strain, respectively. Here, the pre-stretch parameter λ_p is set to 0.8.

on the cylinder, increasing $\hat{\mu}_{\text{cr}}$ as the axial stretch grows. Furthermore, we observe that the critical wavenumber rapidly increases for small $\hat{\Lambda}_s$, and saturates to a constant value when the surface is nearly inextensible. From a physical standpoint, these results suggest that the periodic beading pattern can be triggered more easily when the surface is stiffer and nearly inextensible. We also remark that, as before, the critical wavenumber predicted by the linear stability analysis is finite while the system remains stable for longer wavelengths ($\hat{k} \rightarrow 0$). Thus, periodic patterning appears to be favourable compared to isolated bulging, in agreement with the observations in the experiments (Mora et al., 2010).

We also explore the stability of cylindrical configurations by modulating the surface tension through λ_p . The results are shown in fig. 8. We find again a non-zero critical wavenumber, accordingly with the beading phenomenon. From fig. 9 we can also notice that when $\hat{\mu}$ decreases, the critical threshold for λ_p decreases as well, while the wavenumber sharply increases for small values of $\hat{\mu}$ and saturates at a constant value when the non-dimensional shear modulus is sufficiently large.

Finally, we analyse the stability of the cylindrical configuration with respect to the axial strain λ . As shown in fig. 10, we find a finite positive critical wavenumber, consistently with all other cases explored in this section. Interestingly, the marginal stability curves form closed loops, suggesting that while buckling occurs initially, the system may return to the unbuckled state if λ becomes sufficiently large. This aspect will be investigated in the following through finite element simulations. Moreover, from fig. 11, we notice that both the critical thresholds for λ_p and for the dimensionless wavenumber increase sublinearly as λ is incremented. We observe that the critical wavenumber \hat{k}_{cr} is always between 0.5 and 0.7 in all the cases examined in this section. In the next section, we characterize the post-buckling behaviour of the critical mode in the fully nonlinear regime.

5 Numerical simulations

In this section, we detail the numerical methods and present the results of the simulations for the nonlinear boundary value problem (13a)-(19), both close to the bifurcation threshold and in the post-buckling regime. Readers mainly interested in results are suggested to go directly to section 5.2.

5.1 Weak formulation and finite-element approximation

Since the problem we are studying is axisymmetric, we can simplify our analysis by reducing it to the rectangular domain $\Sigma = (0, L) \times (0, R_0)$ placed in the (Z, R) plane, where $L = 2\pi/(k_{\text{cr}}\lambda)$ is the critical wavelength of the perturbation. The fully 3D solution can be reconstructed by symmetry from the 2D solution on this cylindrical section.

The upper boundary side, i.e. $\Gamma_4 = \{(Z, R) \in \Sigma : 0 \leq Z \leq L, R = R_0\}$, represents the free surface of the cylinder, where the pre-stretched elastic surface is present. The following Dirichlet boundary

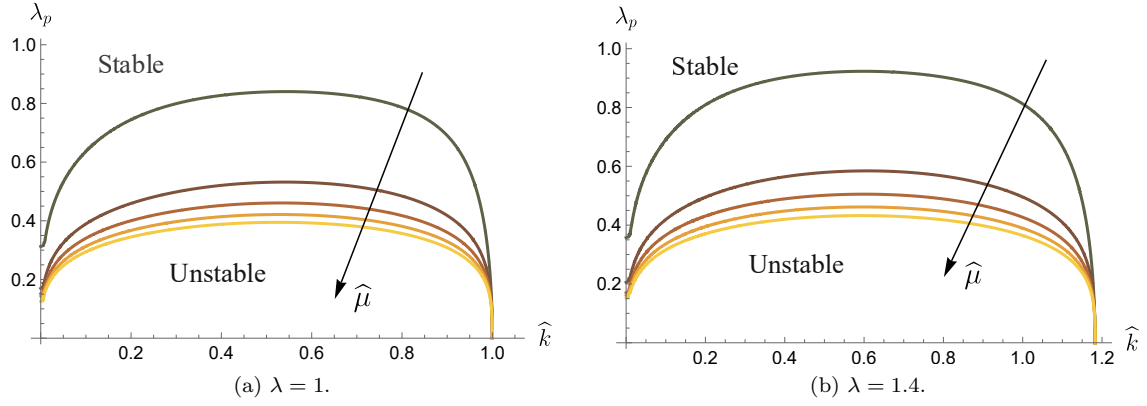


Figure 8: Plot of the pre-stretch parameter λ_p versus the dimensionless wavenumber \hat{k} for unitary (fig. 8a) and nonunitary (fig. 8b) axial strain, respectively. Here, dimensionless surface extensibility $\hat{\Lambda}_s$ is set to 40 and the dimensionless shear modulus $\hat{\mu} = 0.5, 10.5, 20.5, 30.5, 40.5$. The arrow denotes the direction of growth of $\hat{\mu}$.

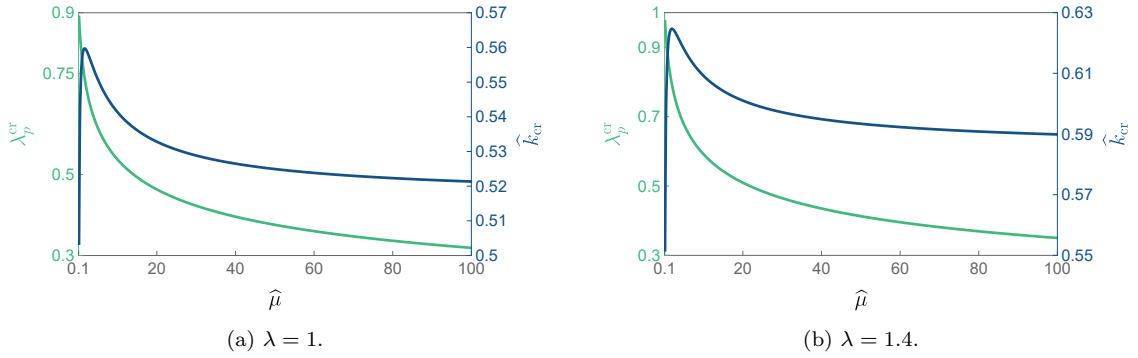


Figure 9: Plot of the critical bifurcation thresholds of the pre-stretch parameter λ_p^{cr} (turquoise) and of the dimensionless wavenumber \hat{k}_{cr} (blue) against the dimensionless shear modulus $\hat{\mu}$ for unitary (fig. 9a) and nonunitary (fig. 9b) axial strain, respectively. Here, the dimensionless surface extensibility $\hat{\Lambda}_s$ is set to 40.

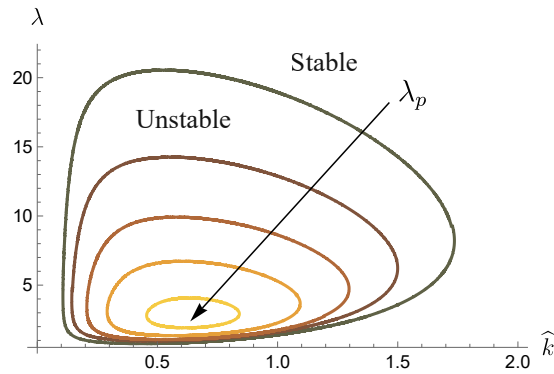


Figure 10: Plot of the axial stretch λ versus the dimensionless wavenumber k . The arrow denotes the direction of growth of the pre-stretch parameter λ_p with uniform steps of amplitude 0.05, from 0.5 to 0.7.

conditions are imposed on the remaining edges

$$\begin{aligned}
 u_Z &= 0 && \text{on } \Gamma_1 = \{(Z, R) \in \Sigma : Z = 0, 0 \leq R \leq R_0\}, \\
 u_Z &= (\lambda - 1)L && \text{on } \Gamma_2 = \{(Z, R) \in \Sigma : Z = L, 0 \leq R \leq R_0\}, \\
 u_R &= 0 && \text{on } \Gamma_3 = \{(Z, R) \in \Sigma : R = 0, 0 \leq Z \leq L\}.
 \end{aligned}$$

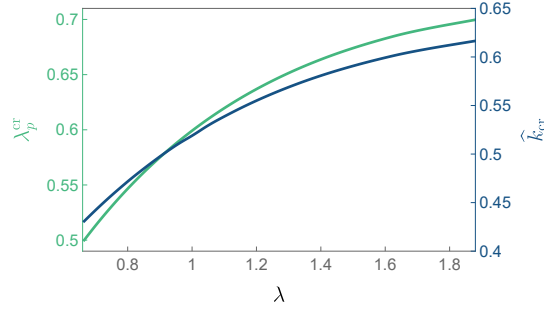


Figure 11: Plot of the critical bifurcation thresholds of the pre-stretch parameter λ_p^{cr} (turquoise) and of the dimensionless wavenumber \hat{k}_{cr} (blue) against the axial strain λ . Here, we set the dimensionless surface extensibility $\hat{\Lambda}_s$ to 10 and the dimensionless shear modulus $\hat{\mu}$ to 0.8.

while homogeneous Neumann conditions are assumed for the remaining component of the traction. In particular, on Γ_1 and Γ_2 roller-type boundary conditions are imposed: the axial displacement is prescribed to enforce the mean stretch λ , while the radial displacement is left free under zero traction. These conditions effectively act as symmetry boundaries, enabling the modelling of a segment of an infinite, uniformly stretched cylinder.

A small imperfection is applied to the mesh close to Γ_4 to initiate the mechanical instability. In order to follow the bifurcated branch, we employ an arclength continuation algorithm (Seydel, 2010), briefly reviewed in the following.

Let us consider the system of parametrized equations stated in an abstract setting

$$\mathbf{f}(\mathbf{y}, \eta) = \mathbf{0}, \quad (38)$$

where \mathbf{y} represents the state of a (physical) system and η is the control parameter of the bifurcation problem. In our application, $\mathbf{y} = (\mathbf{u}, p)$ and η is one of the dimensionless parameters $\hat{\mu}, \lambda$ and λ_p .

Continuation algorithms allow us to find the region of the plane (\mathbf{y}, η) where eq. (38) is satisfied. Specifically, we exploited a pseudo-arclength continuation algorithm, which requires the adoption of the control parameter η as an additional unknown of the system. As a consequence, we must add a further equation to the problem. Assuming that we know that $\mathbf{f}(\mathbf{y}_j, \eta_j) = \mathbf{0}$, we look for a couple $(\mathbf{y}_{j+1}, \eta_{j+1})$ that satisfies eq. (38) and a constraint of the form

$$\|\mathbf{y}_{j+1} - \mathbf{y}_j\|_Y^2 + \|\eta_{j+1} - \eta_j\|_H^2 = ds^2 \quad (39)$$

where ds is the pseudo-arclength parameter and $\|\cdot\|_Y$ and $\|\cdot\|_H$ are suitable norms for \mathbf{y} and η . This equation restricts the search of $(\mathbf{y}_{j+1}, \eta_{j+1})$ to the points that are at a distance ds (in terms of the norms $\|\cdot\|_Y$ and $\|\cdot\|_H$) from the previous solution found at the previous step.

The problem given by eqs. (38) and (39) usually admits multiple solutions. In order to proceed along a specific path in the bifurcation diagram, a predictor-corrector method is frequently exploited. Specifically, assume that at least one solution of eq. (38) can be found, say, (\mathbf{y}_1, η_1) . Then, the j -th continuation step attempts to find the solution $(\mathbf{y}_{j+1}, \eta_{j+1})$ starting from the previously calculated (\mathbf{y}_j, η_j) . This process is usually split into two parts: the former is called *predictor step* and denoted by $(\bar{\mathbf{y}}_{j+1}, \bar{\eta}_{j+1})$. It is aimed at finding a good approximation of $(\mathbf{y}_{j+1}, \eta_{j+1})$ without necessarily being a solution of eq. (38). The latter is named *corrector step* and, starting from the output of the predictor step, will produce an effective solution of eq. (38). It usually consists in a Newton-Rapson algorithm.

$$(\mathbf{y}_j, \eta_j) \xrightarrow{\text{predictor}} (\bar{\mathbf{y}}_{j+1}, \bar{\eta}_{j+1}) \xrightarrow{\text{corrector}} (\mathbf{y}_{j+1}, \eta_{j+1}).$$

This induces the corrector to modify the predictor output in order to find a solution that satisfies eq. (39).

In our application, in eq. (39) for the state $\mathbf{y} = (\mathbf{u}, p)$ and the control parameter η , we adopt the L^2 norm over the referential domain \mathcal{B}_0 . In the simulations presented in this work, we used a secant predictor, i.e

$$(\bar{\mathbf{y}}_{j+1}, \bar{\eta}_{j+1}) = (\mathbf{y}_j, \eta_j) + (\mathbf{y}_j - \mathbf{y}_{j-1}, \eta_j - \eta_{j-1}),$$

meaning that the predictor is chosen on the prolongation of the segment $(\mathbf{y}_j - \mathbf{y}_{j-1}, \eta_j - \eta_{j-1})$.

To introduce the weak formulation of the two-dimensional problem, we define the following functional spaces

$$\begin{aligned}\mathcal{V} &= \left\{ \mathbf{v} \in [H^1(\Sigma)]^2 : v_R = 0 \text{ on } \Gamma_3, v_Z = 0 \text{ on } \Gamma_1, v_Z = (\lambda - 1)L \text{ on } \Gamma_2 \right\}, \\ \mathcal{V}_0 &= \left\{ \mathbf{v} \in [H^1(\Sigma)]^2 : v_R = 0 \text{ on } \Gamma_2 \cup \Gamma_3, v_Z = 0 \text{ on } \Gamma_1 \right\}, \\ \mathcal{Q} &= L^2(\Sigma).\end{aligned}$$

Specifically, \mathcal{V} and \mathcal{V}_0 represent the spaces where the trial and test functions for the displacement, respectively, will be sought, while \mathcal{Q} is the functional space for trial and test functions associated to the pressure field. The parameter space is simply \mathbb{R} . To sum up, the weak formulation of the arclength problem reads: find $(\mathbf{u}_{j+1}, p_{j+1}, \eta_{j+1}) \in \mathcal{V} \times \mathcal{Q} \times \mathbb{R}$ such that

$$\int_{\Sigma} \mathbf{P}_{j+1} : \nabla \mathbf{v} \, dA_0 + \int_{\Gamma_4} \mathbf{P}_{s_{j+1}} : \nabla_s \mathbf{v} \, d\ell_0 = 0 \quad \forall \mathbf{v} \in \mathcal{V}_0, \quad (40a)$$

$$\int_{\Sigma} (\det \mathbf{F}_{j+1} - 1) q \, dA_0 = 0 \quad \forall q \in \mathcal{Q}, \quad (40b)$$

$$\delta \eta \left(\int_{\Sigma} (|\mathbf{u}_{j+1} - \mathbf{u}_j|^2 + (p_{j+1} - p_j)^2) 2R \, dA_0 + (\eta_{j+1} - \eta_j)^2 |\Sigma| R_0 \right) = \delta \eta \, ds^2 |\Sigma| R_0 \quad \forall \delta \eta \in \mathbb{R}, \quad (40c)$$

where the Piola-Kirchhoff tensors and the deformation gradient tensor are evaluated at $(\mathbf{u}, p) = (\mathbf{u}_{j+1}, p_{j+1})$.

We introduce the discretization of the problem by defining an isotropic triangulation $\mathcal{T} = \bigcup_{i=1}^{n_e} \mathcal{K}_i$ over Σ , where, for every i , \mathcal{K}_i is a triangle in Σ and n_e is the total number of triangles. In each simulation, we discretize the computational domain using a structured mesh with 30 elements along the radial direction. Equations (40a) to (40c) are discretized using a stable pair of continuous finite dimensional spaces belonging to the family of Taylor-Hood elements (Quarteroni, 2018). In particular, we use \mathbb{P}^2 elements for the displacement field and \mathbb{P}^1 elements for the pressure over each triangle \mathcal{K}_i in \mathcal{T} , where \mathbb{P}^r denotes the space of polynomials of degree r over the triangle \mathcal{K}_i that are continuous over the physical domain. The proposed numerical scheme is implemented in Python using the finite element computing platform **FEniCS** (Logg et al., 2012) and library **BiFEniCS** that allows to implement the continuation algorithm (Riccobelli et al., 2020).

5.2 Results of the numerical simulation

We start by studying the bifurcations induced in the fully nonlinear problem by variations of the dimensionless shear modulus $\hat{\mu}$. The bifurcation diagram, reported in fig. 12, shows the amplitude of the beading pattern Δr versus the dimensionless shear modulus $\hat{\mu}$, where

$$\Delta r = \max_{Z \in [0, 2\pi R_0 / (\lambda \hat{k}_{cr})]} r(R_0, Z) - \min_{Z \in [0, 2\pi R_0 / (\lambda \hat{k}_{cr})]} r(R_0, Z). \quad (41)$$

The plot in fig. 12 shows that the cylinder undergoes a subcritical pitchfork bifurcation when it reaches the marginal stability threshold predicted by the linear stability analysis. In particular, we notice that the cylindrical configuration remains stable as long as $\hat{\mu}$ is greater than the bifurcation threshold. Nearby the marginal stability threshold, the buckled morphology reproduces the sinusoidal pattern of the linear stability analysis. In the nonlinear regime, the system exhibits the formation of bulges spaced with long, extremely thinned regions: this phenomenon is caused by an increasingly localized beading pattern due to a progressive decrease in $\hat{\mu}$. Structures like these are typically observed in damaged axons, where a similar morphological instability occurs when the degraded cytoskeleton is squeezed by the action of the surrounding actin cortex (Datar et al., 2019; Riccobelli, 2021; Fu et al., 2021; Deghany et al., 2024).

Similarly, we study the behaviour of the cylinder subjected to progressive variations of the pre-stretch parameter λ_p , simulating the increase of surface tension induced by the change of the medium surrounding the cylinder, as in the experiments of Mora et al. (2013). In fig. 13 we show the dimensionless beading amplitude against λ_p . Similarly to $\hat{\mu}$, the bifurcation diagram shows a subcritical pitchfork bifurcation that stabilizes in the nonlinear regime. We deduce that the morphology remains stable in a cylindrical

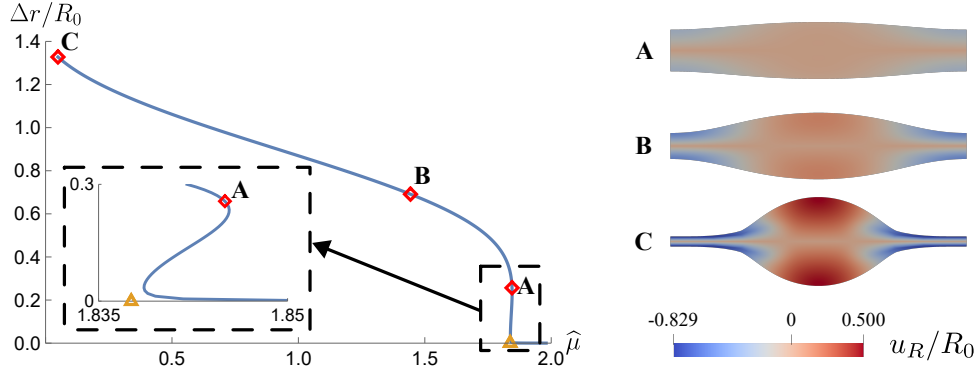


Figure 12: (Left) Bifurcation diagram showing the dimensionless beading amplitude $\Delta r/R_0$ (see Eq. (41)) versus the dimensionless shear modulus $\hat{\mu}$. Here, the axial strain λ , the dimensionless surface extensibility $\hat{\Lambda}_s$, and the pre-stretch parameter λ_p are set to 1.4, 40 and 0.8, respectively. The cylindrical configuration becomes unstable when $\hat{\mu}$ decreases below the critical threshold $\hat{\mu}_{cr}$. The orange triangle denotes the theoretical stability threshold obtained with the linear stability analysis. (Right) Buckled morphology obtained for the three values of $\hat{\mu}$, corresponding to the three points A, B and C reported in the bifurcation diagram.

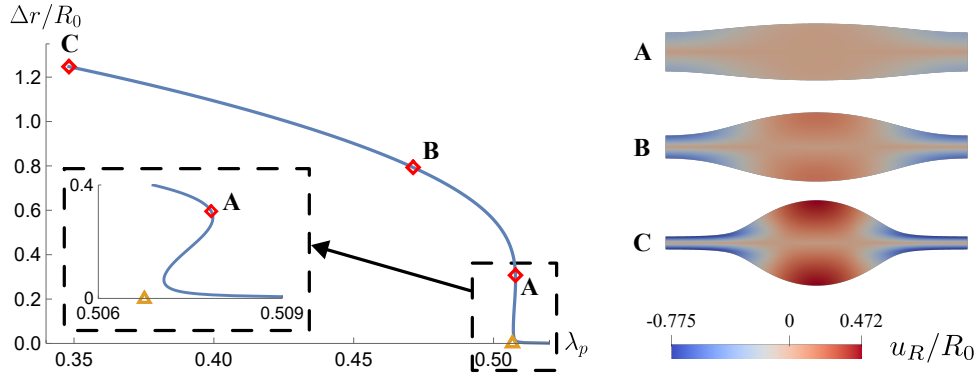


Figure 13: (Left) Bifurcation diagram showing the dimensionless beading amplitude $\Delta r/R_0$ (see Eq. (41)) versus the pre-stretch parameter λ_p . Here, the axial strain λ , the dimensionless surface extensibility $\hat{\Lambda}_s$ and the dimensionless shear modulus $\hat{\mu}$ are set to 1.4, 40 and 20.5, respectively. The cylindrical configuration becomes unstable when λ_p decreases below the critical threshold λ_p^{cr} . The orange triangle denotes the theoretical stability threshold obtained with the linear stability analysis. (Right) Buckled morphology obtained for the three values of λ_p , corresponding to the three points A, B and C reported in the bifurcation diagram.

shape when λ_p is sufficiently high, i.e. for small surface pre-stretch. Close to the bifurcation value, the cylindrical profile begins to deform, leading to a similar periodic beading as in fig. 12. Therefore, a decrease of λ_p corresponds to a more and more pronounced separation between bulges and thinned regions. We recall that the relation between λ_p and surface tension is discussed in Remark 1, and smaller values of λ_p are associated with an increased surface stress.

Finally, we perform the post-buckling simulations by continuously varying the axial strain λ . We notice different behaviors depending on λ_p . As shown in fig. 14, for moderate pre-stretch, we observe a supercritical bifurcation. If the body is further axially stretched, the system returns to the unbuckled cylindrical configuration. This possibility was also explored by Taffetani and Ciarletta (2015a). On the other hand, for smaller values of λ_p , a subcritical pitchfork bifurcation occurs (fig. 14b). In the nonlinear regime, if the cylinder is further stretched, the instability is not suppressed, as in the previous case. Instead, a sequence of period-halving secondary bifurcations appears.

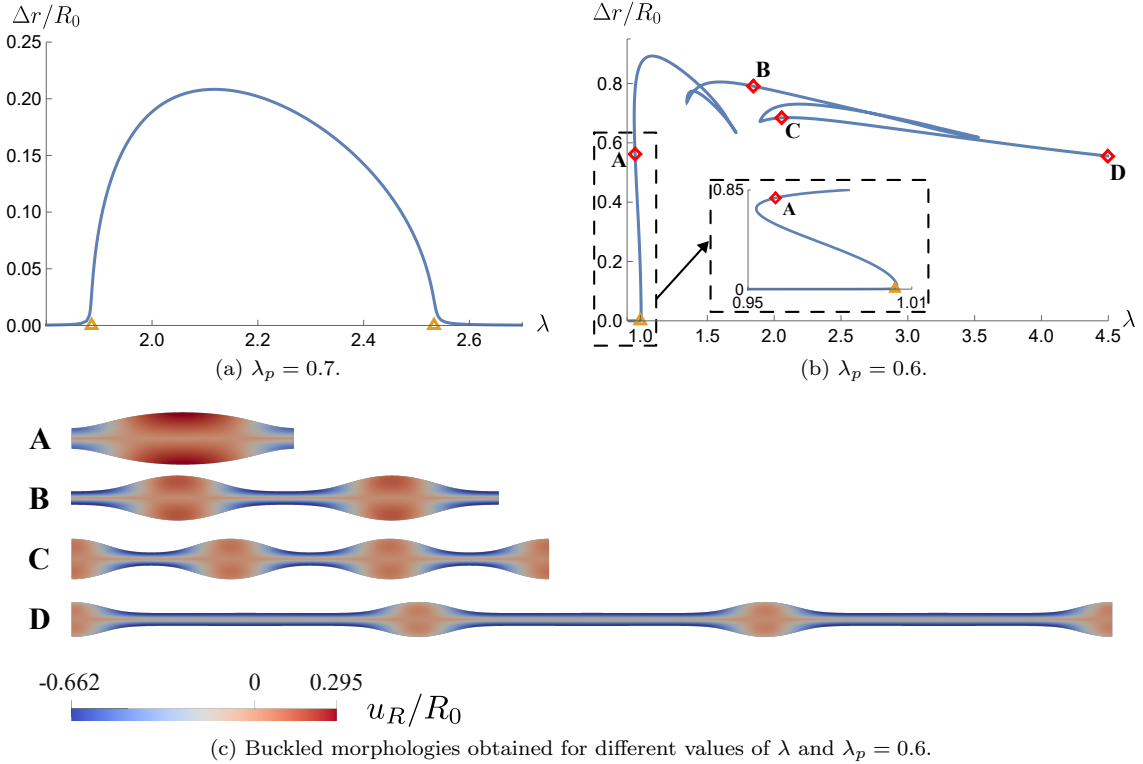


Figure 14: (Top) Bifurcation diagrams showing the dimensionless beading amplitude $\Delta r/R_0$ (see Eq. (41)) versus the axial stretch λ . Here, the dimensionless shear modulus $\hat{\mu}$ and the dimensionless surface extensibility $\hat{\Lambda}_s$ are set to 0.8 and 10, respectively, while the pre-stretch parameter λ_p is equal to 0.7 (a) and 0.6 (b). The orange triangles denote the marginal stability thresholds obtained with the linear stability analysis. (Bottom) Beaded morphology of the buckled cylinder for $\lambda_p = 0.6$, corresponding to the points A, B, C, and D reported in the bifurcation diagram of panel (b).

6 Final remarks

Surface phenomena in soft elastic media have attracted significant attention due to their relevance in material science, biophysics, and engineering. In this work, we have incorporated elastic effects into surface tension to effectively describe the Plateau-Rayleigh instability in solids.

Specifically, we have adopted the theory of material surfaces proposed by Gurtin and Murdoch (1975) to account for elastic pre-stretch. Through linear stability analysis, we have shown that a cylindrical solid can undergo mechanical instability when surface energy is sufficiently high relative to bulk elastic energy. In particular, a mechanical instability can be triggered by

- decreasing bulk elastic stiffness,
- applying axial stretch,
- increasing surface tension.

All these scenarios are thoroughly analysed in section 4, where we prove that the critical wavenumber falls within the interval $0.5R_0 < k_{cr} < 0.7R_0$, R_0 being the reference radius. This range qualitatively aligns with experimental findings from (Matsuo and Tanaka, 1992; Mora et al., 2010) and has not been captured by previous mathematical models, highlighting the crucial role of surface tension elasticity in reproducing this phenomenon. The only exception is provided by Taffetani and Hennessy (2024), which incorporated bending elastic energy alongside a constant surface tension, suggesting that elasticity may play a role in triggering a periodic pattern. We remark that the boundary layer generated by capillary effects is relatively small, meaning that stretching energy should dominate over bending terms, thereby

justifying the approach proposed in this paper. Nevertheless, a promising avenue for exploring the interplay between stretching and bending is offered by the theoretical framework proposed by Tomassetti (2024).

The postbuckling behavior is investigated using a finite element approximation combined with a continuation algorithm, with results presented in section 5. Depending on the parameter values, the resulting buckled states stem from either subcritical or supercritical pitchfork bifurcations. Interestingly, when buckling is induced by axial stretching, we observe either a reversal of the bifurcation, where the system returns to a straight cylindrical configuration after transient buckling at higher stretches, or a sequence of period-halving bifurcations.

The potential role of secondary bifurcations in wavelength selection has been conjectured in Mora et al. (2010) and our study confirms that they play an important role far from the bifurcation threshold, leading to a cascade of period-halving events.

Our work offers a possible explanation for the onset and development of beading in soft elastic filaments and underscores the importance of incorporating strain-dependent surface tension at the interface of soft solids. Indeed, key characteristics of the elastic Rayleigh-Plateau instability, such as the finite wavelength, cannot be captured without accounting for this elastic dependence. Future efforts will be devoted to understanding the behaviour of this system when subjected to structural damage. Hydrogel filaments have been observed to develop voids following mechanical instability (Matsuo and Tanaka, 1992), a phenomenon reminiscent of elastic cavitation. Studying this system may shed light on the structural damage occurring in neurons during neurodegenerative diseases, where similar beaded structures are observed in axons (Pullarkat et al., 2006; Datar et al., 2019). Moreover, an experimental characterization of material surface parameters would be of interest, as has been done for linearly elastic material surfaces in Heyden et al. (2022).

Acknowledgments

This work has been partially supported by INdAM through the project *MATH-FRAC: MATHEMATICAL modelling of FRACTure in nonlinear elastic materials* and by PRIN 2022 project *Mathematical models for viscoelastic biological matter*, Prot. 202249PF73 – Funded by European Union - Next Generation EU - Italian Recovery and Resilience Plan (PNRR) - M4C1_CUP D53D23005610001. Financial support from the Italian Ministry of University and Research (MIUR) through the grant "Dipartimenti di Eccellenza 2023-2027 (Mathematics Area)" is gratefully acknowledged. The authors are members of GNFM – INdAM (National Group of Mathematical Physics).

References

- Ang, I., Liu, Z., Kim, J., Hui, C.-Y., and Bouklas, N. (2020). Effect of elastocapillarity on the swelling kinetics of hydrogels. *Journal of the Mechanics and Physics of Solids*, 145:104132.
- Ang, I., Yousafzai, M. S., Yadav, V., Mohler, K., Rinehart, J., Bouklas, N., and Murrell, M. (2024). Elastocapillary effects determine early matrix deformation by glioblastoma cell spheroids. *APL Bio-engineering*, 8(2).
- Bakiler, A. D., Javili, A., and Dortdivanlioglu, B. (2023). Surface elasticity and area incompressibility regulate fiber beading instability. *Journal of the Mechanics and Physics of Solids*, 176:105298.
- Bevilacqua, G., Shao, X., Saylor, J. R., Bostwick, J. B., and Ciarletta, P. (2020). Faraday waves in soft elastic solids. *Proceedings of the Royal Society A: Mathematical, Physical and Engineering Sciences*, 476(2241).
- Bico, J., Reyssat, É., and Roman, B. (2018). Elastocapillarity: when surface tension deforms elastic solids. *Annual Review of Fluid Mechanics*, 50(1):629–659.
- Bigoni, D. and Gei, M. (2001). Bifurcations of a coated, elastic cylinder. *International Journal of Solids and Structures*, 38(30):5117–5148.

- Chadwick, P. and Ogden, R. W. (1971). A theorem of tensor calculus and its applications to isotropic elasticity. *Archive for Rational Mechanics and Analysis*.
- Ciarletta, P. and Ben Amar, M. (2012). Peristaltic patterns for swelling and shrinking of soft cylindrical gels. *Soft Matter*, 8(6):1760.
- Datar, A., Ameeramja, J., Bhat, A., Srivastava, R., Mishra, A., Bernal, R., Prost, J., Callan-Jones, A., and Pullarkat, P. A. (2019). The roles of microtubules and membrane tension in axonal beading, retraction, and atrophy. *Biophysical Journal* 117.
- Dehghany, M., Naghdabadi, R., Sohrabpour, S., Li, Y., and Hu, Y. (2020). A thermodynamically consistent electro-chemo-mechanical theory for modeling axonal swelling. *Journal of the Mechanics and Physics of Solids*, 145:104113.
- Dehghany, M., Naghdabadi, R., Sohrabpour, S., Li, Y., and Hu, Y. (2024). Osmotically driven beading instability in axons: Continuum theory, perturbation analysis and finite element implementation. *International Journal of Engineering Science*, 194:103971.
- Elettro, H., Neukirch, S., Vollrath, F., and Antkowiak, A. (2016). In-drop capillary spooling of spider capture thread inspires hybrid fibers with mixed solid-liquid mechanical properties. *Proceedings of the National Academy of Sciences*, 113(22):6143–6147.
- Fu, Y., Jin, L., and Goriely, A. (2021). Necking, beading, and bulging in soft elastic cylinders. *Journal of the Mechanics and Physics of Solids*, 147:104250.
- Giudici, A. and Biggins, J. S. (2020). Ballooning, bulging, and necking: An exact solution for longitudinal phase separation in elastic systems near a critical point. *Physical Review E*, 102(3).
- Goriely, A., Vandiver, R., and Destrade, M. (2008). Nonlinear euler buckling. *Proceedings of the Royal Society A: Mathematical, Physical and Engineering Sciences*, 464(2099):3003–3019.
- Gurtin, M. E. and Murdoch, A. I. (1975). A continuum theory of elastic material surfaces. *Archive for Rational Mechanics and Analysis*.
- Heyden, S., Vlahovska, P. M., and Dufresne, E. R. (2022). A robust method for quantification of surface elasticity in soft solids. *Journal of the Mechanics and Physics of Solids*, 161:104786.
- Holland, M. A., Kosmata, T., Goriely, A., and Kuhl, E. (2013). On the mechanics of thin films and growing surfaces. *Mathematics and Mechanics of Solids*.
- Javili, A., McBride, A., Steinmann, P., and Reddy, B. D. (2014). A unified computational framework for bulk and surface elasticity theory: a curvilinear-coordinate-based finite element methodology. *Computational Mechanics*.
- Lestringant, C. and Audoly, B. (2020). A one-dimensional model for elasto-capillary necking. *Proceedings of the Royal Society A*, 476(2240):20200337.
- Logg, A., Mardal, K.-A., and Wells, G. N. (2012). *Automated Solution of Differential Equations by the Finite Element Method*. Springer.
- Matsuo, E. S. and Tanaka, T. (1992). Patterns in shrinking gels. *Nature*, 358(6386):482–485.
- Mora, S., Maurini, C., Phou, T., Fromental, J.-M., Audoly, B., and Pomeau, Y. (2013). Solid drops: Large capillary deformations of immersed elastic rods. *Physical Review Letters*, 111(11).
- Mora, S., Phou, T., Fromental, J.-M., Pismen, L. M., and Pomeau, Y. (2010). Capillarity driven instability of a soft solid. *Physical Review Letters*, 105:214301.
- Mora, S., Phou, T., Fromental, J.-M., and Pomeau, Y. (2014). Gravity driven instability in elastic solid layers. *Physical Review Letters*, 113(17).

- Naraghi, M., Chasiotis, I., Kahn, H., Wen, Y., and Dzenis, Y. (2007). Mechanical deformation and failure of electrospun polyacrylonitrile nanofibers as a function of strain rate. *Applied Physics Letters*, 91(15).
- Ogden, R. W. (1997). *Non-linear elastic deformations*. Courier Corporation.
- Piriz, A. R., López Cela, J. J., and Tahir, N. A. (2009). Linear analysis of incompressible Rayleigh-Taylor instability in solids. *Physical Review E*, 80(4).
- Plateau, J. (1873). *Statique expérimentale et théorique des liquides soumis aux seules forces moléculaires*. Gauthier-Villars.
- Plohr, B. and Sharp, D. (1998). Instability of accelerated elastic metal plates. *Zeitschrift für angewandte Mathematik und Physik*, 49(5):786.
- Pullarkat, P. A., Dommersnes, P., Fernández, P., Joanny, J.-F., and Ott, A. (2006). Osmotically driven shape transformations in axons. *Physical Review Letters*, 96(4).
- Py, C., Reverdy, P., Doppler, L., Bico, J., Roman, B., and Baroud, C. N. (2007). Capillary origami: spontaneous wrapping of a droplet with an elastic sheet. *Physical Review Letters*, 98(15):156103.
- Quarteroni, A. (2018). *Numerical Models for Differential Problems*. Springer.
- Rayleigh, L. (1892). On the instability of a cylinder of viscous liquid under capillary force. *The London, Edinburgh, and Dublin Philosophical Magazine and Journal of Science*, 34(207):145–154.
- Riccobelli, D. (2021). Active elasticity drives the formation of periodic beading in damaged axons. *Physical Review E*, 104(2):024417.
- Riccobelli, D. (2025). Surface tension-driven boundary growth in tumour spheroids. *Interface Focus*, accepted for publication.
- Riccobelli, D. and Bevilacqua, G. (2020). Surface tension controls the onset of gyrification in brain organoids. *Journal of the Mechanics and Physics of Solids*, 134:103745.
- Riccobelli, D. and Ciarletta, P. (2017). Rayleigh–Taylor instability in soft elastic layers. *Philosophical Transactions of the Royal Society A: Mathematical, Physical and Engineering Sciences*, 375(2093):20160421.
- Riccobelli, D., Noselli, G., and DeSimone, A. (2020). Rods coiling about a rigid constraint: Helices and perversions. *Proceedings of the Royal Society A: Mathematical, Physical and Engineering*, 477(2246), 20200817.
- Robinson, A. C. and Swegle, J. W. (1989). Acceleration instability in elastic-plastic solids. ii. analytical techniques. *Journal of Applied Physics*, 66(7):2859–2872.
- Seydel, R. (2010). *Practical Bifurcations and Stability Analysis*. Springer.
- Shao, X., Bevilacqua, G., Ciarletta, P., Saylor, J. R., and Bostwick, J. B. (2020). Experimental observation of faraday waves in soft gels. *Physical Review E*, 102(6).
- Shao, X., Saylor, J. R., and Bostwick, J. B. (2018). Extracting the surface tension of soft gels from elastocapillary wave behavior. *Soft Matter*, 14(36):7347–7353.
- Shuttleworth, R. (1950). The surface tension of solids. *Proceedings of the physical society. Section A*, 63(5):444.
- Style, R. W., Jagota, A., Hui, C.-Y., and Dufresne, E. R. (2017). Elastocapillarity: surface tension and the mechanics of soft solids. *Annual Review of Condensed Matter Physics*, 8(1):99–118.
- Taffetani, M. and Ciarletta, P. (2015a). Beading instability in soft cylindrical gels with capillary energy: Weakly non-linear analysis and numerical simulations. *Journal of the Mechanics and Physics of Solids*, 81:91–120.

- Taffetani, M. and Ciarletta, P. (2015b). Elastocapillarity can control the formation and the morphology of beads-on-string structures in solid fibers. *Physical Review E*, 91(3):032413.
- Taffetani, M. and Hennessy, M. G. (2024). Curvature controls beading in soft coated elastic cylinders: Finite wavemode instability and localized modulations. *Journal of the Mechanics and Physics of Solids*, 187:105606.
- Tomassetti, G. (2024). A coordinate-free guide to the mechanics of thin shells. *Mechanics of Materials*, 192:104961.
- Xuan, C. and Biggins, J. (2016). Finite-wavelength surface-tension-driven instabilities in soft solids, including instability in a cylindrical channel through an elastic solid. *Physical Review E*, 94(2):023107.
- Yadav, V., Yousafzai, M. S., Amiri, S., Style, R. W., Dufresne, E. R., and Murrell, M. (2022). Gradients in solid surface tension drive marangoni-like motions in cell aggregates. *Physical Review Fluids*, 7(3):L031101.
- Yu, X. and Fu, Y. (2025). On the incremental equations in surface elasticity. *Mathematics and Mechanics of Solids*, 30(2):470–489.
- Zuo, W., Zhu, M., Yang, W., Yu, H., Chen, Y., and Zhang, Y. (2005). Experimental study on relationship between jet instability and formation of beaded fibers during electrospinning. *Polymer Engineering & Science*, 45(5):704–709.

A Differential operators in curvilinear coordinates

In this appendix we suppose that indices i and j run from 1 to 3, while α and β run from 1 to 2. We denote by $\mathcal{E} = \{\mathbf{e}_1, \mathbf{e}_2, \mathbf{e}_3\}$ the canonical basis of \mathbb{R}^3 . Let $\mathcal{G} = \{\mathbf{g}_1, \mathbf{g}_2, \mathbf{g}_3\}$ be an arbitrary basis in \mathcal{E} . We say that $\mathcal{G}^* = \{\mathbf{g}^1, \mathbf{g}^2, \mathbf{g}^3\}$ is the dual basis to \mathcal{G} if and only if $\mathbf{g}_i \cdot \mathbf{g}^j = \delta_i^j$ for every i and j , where δ_i^j denotes the Kronecker delta. Duality is a reflexive property and, given the basis \mathcal{G} , there always exists its dual \mathcal{G}^* . It is straightforward to see that $\mathcal{E}^* = \mathcal{E}$.

Given an arbitrary vector \mathbf{v} , we denote by $\{v_1, v_2, v_3\}$ its *covariant components* and by $\{v^1, v^2, v^3\}$ its *contravariant components*. Let us assume that $\{\mathbf{g}^1, \mathbf{g}^2, \mathbf{g}^3\}$ be the basis of a generic curvilinear coordinates system $\{\xi^1, \xi^2, \xi^3\}$ and let $d\mathbf{r}$ denote an arbitrary infinitesimal vector expressed in terms of the Cartesian coordinates $\{x^1, x^2, x^3\}$. It is always possible to express $d\mathbf{r}$ in terms of the curvilinear coordinates $\{\xi^1, \xi^2, \xi^3\}$ through the linear, invertible relation $\boldsymbol{\alpha}$ between the two coordinates systems, that is $\mathbf{e}_i = \alpha_i^j \mathbf{g}^j$. The relation between $\mathbf{g}_i, \mathbf{g}^i$ and $d\mathbf{r}$ are expressed as

$$\mathbf{g}_i = \frac{\partial \mathbf{r}}{\partial \xi^i}, \quad \mathbf{g}^i = \frac{\partial \xi^i}{\partial \mathbf{r}}.$$

Moreover, we denote by g^{ij} the map from the contravariant basis to the covariant one and by g_{ij} the mapping from the covariant basis to the contravariant one, namely

$$\begin{aligned} \mathbf{g}^i &= g^{ij} \mathbf{g}_j, \\ \mathbf{g}_i &= g_{ij} \mathbf{g}^j. \end{aligned}$$

The coefficients of these two maps are called covariant and contravariant metric coefficients, respectively. They are defined as $g_{ij} = \mathbf{g}_i \cdot \mathbf{g}_j$ and $g^{ij} = \mathbf{g}^i \cdot \mathbf{g}^j$ and are such that $[g_{ij}] = [g^{ij}]^{-1}$. We can introduce the gradient and divergence operators using the general curvilinear coordinates introduced above (Javili et al., 2014)

$$\text{grad} \{ \cdot \} = \frac{\partial \{ \cdot \}}{\partial \xi^i} \otimes \mathbf{g}_i, \quad (42a)$$

$$\text{div} \{ \cdot \} = \frac{\partial \{ \cdot \}}{\partial \xi^i} \cdot \mathbf{g}_i = \text{grad} \{ \cdot \} : \mathbf{I}, \quad (42b)$$

where \mathbf{l} is the identity tensor in \mathbb{R}^3 .

Let us consider a regular surface \mathcal{S} in the current configuration. Being $\mathcal{P} = (\hat{\xi}^1, \hat{\xi}^2) \subset \mathbb{R}^2$, let $\boldsymbol{\xi} : \mathcal{P} \rightarrow \mathcal{S}$ be a parametrization of the surface. In analogy to the procedure derived for the bulk, we define the covariant and contravariant surface basis vectors for the curvilinear coordinates as

$$\hat{\mathbf{g}}_\alpha = \frac{\partial \mathbf{r}}{\partial \hat{\xi}^\alpha}, \quad \hat{\mathbf{g}}^\alpha = \frac{\partial \hat{\xi}^\alpha}{\partial \mathbf{r}}.$$

As for the bulk, there exists an invertible relation between co- and contravariant surface basis vectors, that is

$$\begin{aligned} \hat{\mathbf{g}}^\alpha &= \hat{g}^{\alpha\beta} \hat{\mathbf{g}}_\beta, \\ \hat{\mathbf{g}}_\alpha &= \hat{g}_{\alpha\beta} \hat{\mathbf{g}}^\beta, \end{aligned}$$

where $[\hat{g}_{\alpha\beta}] = [\hat{g}^{\alpha\beta}]^{-1}$ with $\hat{g}_{\alpha\beta} = \hat{\mathbf{g}}_\alpha \cdot \hat{\mathbf{g}}_\beta$ and $\hat{g}^{\alpha\beta} = \hat{\mathbf{g}}^\alpha \cdot \hat{\mathbf{g}}^\beta$. Now, it is possible to define the contra- and covariant base vectors that are normal to the surface \mathcal{S} as $\hat{\mathbf{g}}^3 := \hat{\mathbf{g}}^1 \wedge \hat{\mathbf{g}}^2$ and $\hat{\mathbf{g}}_3 = [\hat{g}^{33}]^{-1} \hat{\mathbf{g}}^3$ in such a way that

$$\hat{\mathbf{g}}_3 \cdot \hat{\mathbf{g}}^3 = 1,$$

coherently with the definition of dual basis. As a consequence, the normal unit vector to the surface is

$$\mathbf{n} = \frac{\hat{\mathbf{g}}_3}{|\hat{\mathbf{g}}_3|} = \frac{\hat{\mathbf{g}}^3}{|\hat{\mathbf{g}}^3|}, \quad (43)$$

where the last equality holds since $\hat{\mathbf{g}}_3$ and $\hat{\mathbf{g}}^3$ are parallel. The surface identity tensor in the current configuration is defined as

$$\mathbf{H}_s = \mathbf{l} - \hat{\mathbf{g}}_3 \otimes \hat{\mathbf{g}}^3 = \mathbf{l} - \mathbf{n} \otimes \mathbf{n}, \quad (44)$$

that is exactly eq. (2).

We can finally define the surface gradient, divergence and determinant operators as (Javili et al., 2014)

$$\text{grad}_s \{ \cdot \} = \frac{\partial \{ \cdot \}}{\partial \hat{\xi}^\alpha} \otimes \hat{\mathbf{g}}_\alpha, \quad (45a)$$

$$\text{div}_s \{ \cdot \} = \frac{\partial \{ \cdot \}}{\partial \hat{\xi}^\alpha} \cdot \hat{\mathbf{g}}_\alpha = \text{grad}_s \{ \cdot \} : \mathbf{H}_s, \quad (45b)$$

$$\det_s \{ \cdot \} = \frac{|[\{ \cdot \} \cdot \hat{\mathbf{g}}_1] \wedge [\{ \cdot \} \cdot \hat{\mathbf{g}}_2]|}{|\hat{\mathbf{g}}_1 \wedge \hat{\mathbf{g}}_2|}. \quad (45c)$$

To conclude, the *surface divergence theorem* holds: let σ be a regular subsurface of \mathcal{S} with a smooth boundary $\partial\sigma$ and let \mathbf{m} be the outward unit normal to $\partial\sigma$. Then

$$\int_\sigma \mathbf{T} \cdot \mathbf{m} = \int_{\partial\sigma} \text{div}_s \mathbf{T}, \quad (46)$$

for every tangent field \mathbf{T} to σ . In the computations and definitions of this appendix we have exploited the notation we have used for material bodies and surfaces in the current configuration. Nonetheless, all these results are general and can be applied to every framework. However, particular attention should be devoted to the surface identity tensors: if on one hand the reference and actual bulk identities are invariant and equal (Javili et al., 2014), the same cannot be stated for the surface ones. Indeed, while the surface actual identity has been defined in eq. (44), given a surface \mathcal{S}_0 in reference configuration, we have

$$\mathbf{l}_s = \mathbf{l} - \mathbf{N} \otimes \mathbf{N},$$

where \mathbf{N} is the normal unit vector to \mathcal{S}_0 . Since, in general, $\mathcal{S}_0 \neq \mathcal{S}$, also $\mathbf{N} \neq \mathbf{n}$. Thus, we conclude that in general $\mathbf{l}_s \neq \mathbf{H}_s$.

B Coefficients of the matrix M

In this appendix we provide the explicit expressions of the components of the 2×2 matrix M arising from the imposition of the boundary condition eq. (27c). Since the expression for $U(r)$ depends on the value of λ (see eqs. (34) and (36)) we distinguish the two cases.

When $\lambda = 1$ we obtain

$$\begin{aligned}
M_{11} &= J_1(kR_0) (2\lambda_p^4(-2\mu R_0 + \Lambda_s + 2\mu_s) - k^2(\lambda_p^2 - 1)R_0^2(\lambda_p^2\Lambda_s + \Lambda_s + 2\lambda_p^2\mu_s)) + \\
&\quad + kR_0J_0(kR_0) (2\lambda_p^2(2\lambda_p^2\mu R_0 - \lambda_p^2\mu_s + \mu_s) - (\lambda_p^4 + 1)\Lambda_s), \\
M_{12} &= -R_0(J_0(kR_0) (\Lambda_s(k^2(\lambda_p^4 - 1)R_0^2 + 2) + 2\lambda_p^2\mu_s(k^2(\lambda_p^2 - 1)R_0^2 - 2)) + \\
&\quad + kR_0J_1(kR_0) (-4\lambda_p^4\mu R_0 + \lambda_p^4\Lambda_s + \Lambda_s + 2\lambda_p^4\mu_s - 2\lambda_p^2\mu_s)), \\
M_{21} &= k(kR_0J_0(kR_0) ((\lambda_p^4 + 1)\Lambda_s + 2(\lambda_p^2 + 1)\lambda_p^2\mu_s) + \\
&\quad - J_1(kR_0) (-4\lambda_p^4\mu R_0 + \lambda_p^4\Lambda_s + \Lambda_s + 2\lambda_p^4\mu_s - 2\lambda_p^2\mu_s)), \\
M_{22} &= R_0(J_1(kR_0) (k^2R_0(\lambda_p^4\Lambda_s + \Lambda_s + 2\lambda_p^4\mu_s + 2\lambda_p^2\mu_s) + 4\lambda_p^4\mu) + \\
&\quad + kJ_0(kR_0) (4\lambda_p^4\mu R_0 + \lambda_p^4\Lambda_s + \Lambda_s + 2\lambda_p^4\mu_s + 6\lambda_p^2\mu_s)).
\end{aligned}$$

If $\lambda \neq 1$, we get

$$\begin{aligned}
M_{11} &= \frac{1}{\lambda^3} \left(-2J_1(k\lambda R_0) (k^2R_0^2(2\lambda^2\lambda_p^2\mu_s + \lambda\Lambda_s - (\lambda_p^4(\Lambda_s + 2\mu_s)))) - \lambda^2\Lambda_s + \lambda\lambda_p^4(\Lambda_s + 2\mu_s) + 2\lambda_p^2\mu_s \right) + \\
&\quad + k\lambda R_0J_0(k\lambda R_0) (-2\lambda_p^2(2\lambda_p^2\mu R_0 + \mu_s) + \lambda^2\Lambda_s + \lambda\lambda_p^4(\Lambda_s + 2\mu_s)) + \\
&\quad + k\lambda R_0J_2(k\lambda R_0) (-2\lambda_p^2(2\lambda_p^2\mu R_0 + \mu_s) + \lambda^2\Lambda_s + \lambda\lambda_p^4(\Lambda_s + 2\mu_s)), \\
M_{12} &= \frac{1}{\lambda^2} \left(2\sqrt{\lambda}J_1\left(\frac{kR_0}{\sqrt{\lambda}}\right) (k^2R_0^2(2\lambda^2\lambda_p^2\mu_s + \lambda\Lambda_s - (\lambda_p^4(\Lambda_s + 2\mu_s)))) + \right. \\
&\quad + 2\lambda^3\lambda_p^4\mu R_0 - 2\lambda_p^4\mu R_0 - \lambda^2\Lambda_s + \lambda\lambda_p^4(\Lambda_s + 2\mu_s) + 2\lambda_p^2\mu_s + \\
&\quad + kR_0J_0\left(\frac{kR_0}{\sqrt{\lambda}}\right) (2\lambda^3\lambda_p^4\mu R_0 + 2\lambda_p^2(\lambda_p^2\mu R_0 + \mu_s) - \lambda^2\Lambda_s - \lambda\lambda_p^4(\Lambda_s + 2\mu_s)) + \\
&\quad \left. + kR_0J_2\left(\frac{kR_0}{\sqrt{\lambda}}\right) (2\lambda^3\lambda_p^4\mu R_0 + 2\lambda_p^2(\lambda_p^2\mu R_0 + \mu_s) - \lambda^2\Lambda_s - \lambda\lambda_p^4(\Lambda_s + 2\mu_s)) \right), \\
M_{21} &= \frac{k}{\lambda^{3/2}} \left(4(\lambda^3 + 1)\lambda_p^2J_1(k\lambda R_0) (\lambda_p^2\mu R_0 + \mu_s) + k\lambda^2R_0J_0(k\lambda R_0) (2\lambda^2\lambda_p^2\mu_s + \lambda\Lambda_s + \lambda_p^4(\Lambda_s + 2\mu_s)) \right) + \\
&\quad + k\lambda^2R_0J_2(k\lambda R_0) (2\lambda^2\lambda_p^2\mu_s + \lambda\Lambda_s + \lambda_p^4(\Lambda_s + 2\mu_s)), \\
M_{22} &= \frac{k}{\lambda^{5/2}} \left(4\lambda\lambda_p^2J_1\left(\frac{kR_0}{\sqrt{\lambda}}\right) (2\lambda_p^2\mu R_0 + \lambda^3\mu_s + \mu_s) + \right. \\
&\quad + k\lambda^{3/2}R_0J_0\left(\frac{kR_0}{\sqrt{\lambda}}\right) (2\lambda^2\lambda_p^2\mu_s + \lambda\Lambda_s + \lambda_p^4(\Lambda_s + 2\mu_s)) + \\
&\quad \left. + k\lambda^{3/2}R_0J_2\left(\frac{kR_0}{\sqrt{\lambda}}\right) (2\lambda^2\lambda_p^2\mu_s + \lambda\Lambda_s + \lambda_p^4(\Lambda_s + 2\mu_s)) \right).
\end{aligned}$$